Passive radiative cooling and other photonic approaches for the temperature control of photovoltaics: a comparative study for crystalline silicon-based architectures

GEORGE PERRAKIS,[1,2,*] **ANNA C. TASOLAMPROU,**[1] **GEORGE KENANAKIS,**[1] **ELEFTHERIOS N. ECONOMOU,**[1,3] **STELIOS TZORTZAKIS,**[1,2,4] [iD] **AND MARIA KAFESAKI**[1,2]

[1]*Institute of Electronic Structure and Laser (IESL), Foundation for Research and Technology-Hellas (FORTH), 70013 Heraklion, Crete, Greece*
[2]*Dept. of Materials Science and Technology, Univ. of Crete, Heraklion, Greece*
[3]*Department of Physics, University of Crete GR-71003, Heraklion, Crete, Greece*
[4]*Science Program, Texas A&M University at Qatar, P.O. Box 23874, Doha, Qatar*
[*]*gperrakis@iesl.forth.gr*

Abstract: The radiative cooling of objects during daytime under direct sunlight has recently been shown to be significantly enhanced by utilizing nanophotonic coatings. Multilayer thin film stacks, 2D photonic crystals, etc. as coating structures improved the thermal emission rate of a device in the infrared atmospheric transparency window reducing considerably devices' temperature. Due to the increased heating in photovoltaic (PV) devices – that has significant adverse consequences on both their efficiency and life-time – and inspired by the recent advances in daytime radiative cooling, we developed a coupled thermal-electrical modeling to examine the physical mechanisms on how a radiative cooler affects the overall efficiency of commercial photovoltaic modules and how the radiative cooling impact is compared with the impact of other photonic strategies for reducing heat generation within PVs, such as ultraviolet and sub-bandgap reflection. Employing our modeling, which takes into account all the major intrinsic processes affected by the temperature variation in a PV device, we additionally identified the validity regimes of the currently existing PV-cooling models which treat the PV coolers as simple thermal emitters. Finally, we assessed some realistic photonic coolers from the literature, compatible with photovoltaics, to implement the radiative cooling requirements and the requirements related to the reduction of heat generation, and demonstrated their associated impact on the temperature reduction and PV efficiency. Consistent with previous works, we showed that combining radiative cooling with sub-bandgap reflection proves to be more promising for increasing PVs' efficiency. Providing the physical mechanisms and requirements for reducing PV operating temperature, our study provides guidelines for utilizing suitable photonic structures for enhancing the efficiency and the lifetime of PV devices.

1. Introduction

A solar cell operating under the sun inevitably generates heat apart from electrical power. Principally, the highest fraction of the absorbed sunlight remains unexploited as it was explained by Shockley and Queisser in their seminal paper [1] in 1961. According to their analysis, a single-junction silicon-based (semiconductor material with a band-gap of ~1.1 eV) solar cell has a theoretical upper limit for incident solar to electrical power conversion efficiency of around 32%, assuming that it operates at a constant temperature equal to 300 K. In practice, residual power dissipates mainly into heat [2,3] that increases the operating temperature of the solar cell, leading to substantial adverse consequences not only for the lifetime of the materials, but also for the

efficiency of the system mainly due to the increased carrier recombination at elevated temperatures [4]. The heating problem becomes even more prominent in conventional photovoltaic systems (PVs) due to the accumulated heat that arises from the parasitic absorption of incident photons at the various parts of the PV device [see Fig. 1(a)] other than the semiconductor material. This occurs not only at the wavelengths within the absorption band of the semiconductor (for silicon: ~0.28-1.1 μm) but also beyond these wavelengths (sub-bandgap radiation, ~1.1-4 μm, which is a heat source) where the sun still has considerable intensity. As a result, typical operating temperatures [5] can reach values even higher than ~325 K. Indicatively, for a crystalline silicon solar cell, every 1 K temperature rise leads to a relative efficiency decline [6] of about 0.45%. Moreover, the aging rate of a solar cell array doubles for every 10 K solar cell temperature increase [7].
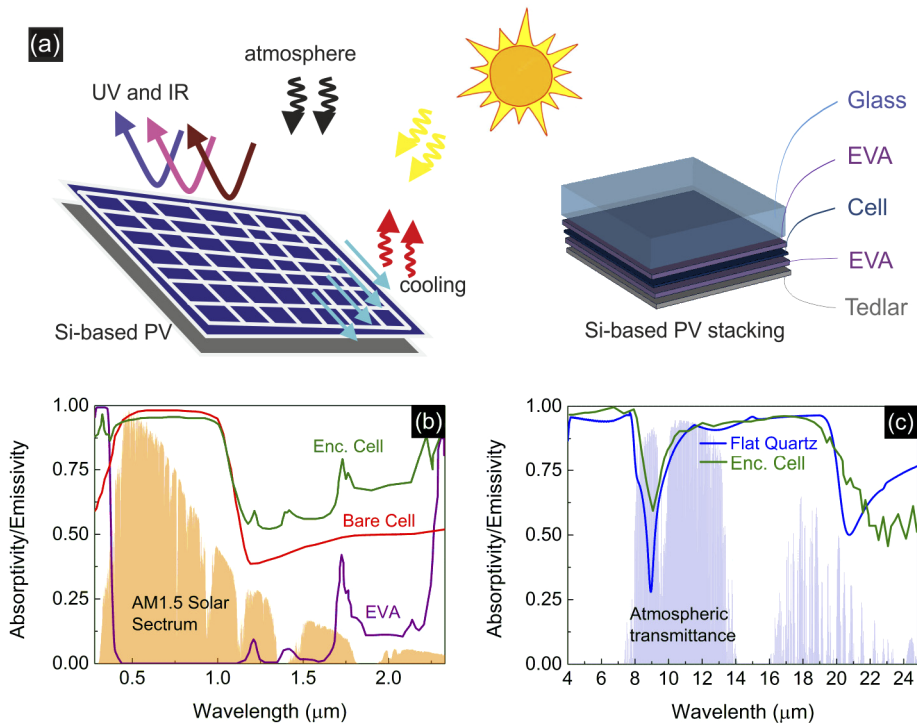

Fig. 1. (a) Schematic of the cooling approaches for the radiative thermal management of PVs and material stacking of the encapsulated crystalline silicon-based PV. The thickness and role of the different layers of the PV module are discussed in the main text. (b) Absorptivity of the bare cell (red line), encapsulated cell (green line), and of a 0.46 mm thick EVA wafer (purple line). Data are extracted from Refs. [15,23,24]. (c) Emissivity spectra in the thermal wavelengths (mid-IR) of a 3.2 mm thick glass (fused Quartz) layer (blue line), compared to the emissivity of the encapsulated cell in (b) (green line).

The significant adverse consequences of the temperature rise on the solar cells have led to the utilization of several cooling approaches. Conventional strategies for cooling are mainly focused on nonradiative heat transfer via conduction or convection, like forced air flow [8], water cooling [9], heat-pipe-based systems [10], etc., most of which consume extra energy. Recently though, there has been a significant advance in the field of passive (i.e., no extra energy input needed) radiative cooling, targeting though mainly cooling of buildings. Raman et al. [11] in 2014 developed a passive radiative cooling system based on a photonic crystal. The photonic crystal was designed to reflect the solar heating power (~0.28-4 μm) and at the same time allow radiative

cooling through thermal emission in the mid-IR, at the atmospheric transparency window of 8-13 μm. In this way the system had radiative access to the coldness of the universe, through this atmospheric transparency window, and therefore could additionally use the universe as a heat sink, with much lower temperature (~3 K) than that of the atmosphere (~300 K). With this approach Raman et al. [11] demonstrated an impressive cooling, up to 5 K under direct sunlight. Subsequently, appropriate passive radiative coolers were designed compatible with PV systems, mainly Si-based PVs, that allowed radiative cooling through enhanced thermal emission in the mid-IR [12–14] but at the same time increased the visible light to go through and reach the PV cells [15,16] for only a certain beneficial spectral window (~0.375-1.1 μm), i.e. via enhancing the transmission in this spectral window while reflecting detrimental UV (~0.28-0.375 μm) and sub-bandgap parasitic (~1.1-4 μm) absorption. The latter approach is particularly important, since the infrared performance of antireflection coatings that only increase PV's transmissivity [17], and hence do not provide sub-bandgap reflection, may have detrimental thermal effects [18]. In this way, the perspective of PV-coolers with a double-role has been demonstrated; both increasing the solar cell absorptivity and also reducing the operating temperature of the device up to ~5.7 K [15].

As highlighted also in Ref. [15], there are currently two major photonic approaches for the thermal management of PVs, focusing on controlling either (i) the solar absorption by reflecting parasitic UV, sub-bandgap radiation [18–20] and further enhancing the beneficial optical absorption, or (ii) the thermal radiation emission. Most of the existing studies employing these approaches though treat PVs as solar absorbers and not as quantum devices, i.e., they do not consider the generation of electrical power by the PV, neither all the major temperature-dependent recombination mechanisms of the generated carriers. This, depending on the operation conditions, may lead to an overestimation of the efficiency increase related to the temperature reduction. In our work, we propose a theoretical thermal-electrical co-model, which takes into account all the major intrinsic processes affected by the temperature variation in a PV device, to examine how a photonic cooler affects the overall efficiency of a realistic PV system. In this respect, we analyze the physical mechanisms [15,18–20], of the efficiency enhancement related to the temperature reduction in PVs further confirming previous results [18–20], and we distinguish and evaluate the impact of each of the previously mentioned photonic approaches [15,20], if implemented both separately and together, on the efficiency enhancement of a PV operating outdoors. Exploiting our model, and particularly its potential to give the impact on the PV efficiency of any different part of the electromagnetic spectrum, we exploit, among others, the considerable impact [2,3] of the thermalization losses (i.e., excess energy of incident photons relative to the bandgap of the semiconductor that cannot be exploited and finally dissipates into heat) on the PV efficiency. Finally, we examine some realistic photonic structures proposed in the literature towards the implementation and fulfillment of the radiative cooling requirements, and we analyze their impact on the PV's electrical properties, in comparison also with our evaluated "ideal cooler".

2. Features of solar cell operation in outdoor conditions

In the present work we study crystalline silicon-based solar cells such as the ones that are currently on the market of solar cell technology [21]. A typical state-of-the-art silicon-based photovoltaic module along with each interlayer is shown in Fig. 1(a).

The most important part of the PV module is the cell, where the conversion of the incident solar power to electricity takes place. We assume that the cell involves a 250 μm thick mono-crystalline silicon wafer with interdigitated state-of-the-art type back contacts (IBC) responsible for collecting the photo-generated carriers [22]. All remaining layers, other than the cell, are required for its stable operation. More specifically, the transparent top surface, most often a 3.2 mm thick glass (contains 70−80% silica in addition to other materials like Al_2O_3, Na_2O, CaO, etc.), protects the exposed solar cell system from the outside conditions and provides mechanical

strength and rigidity. The most common encapsulant, the EVA (ethylene-vinyl acetate), is used as a 0.46 mm thick joint that provides adhesion between the cells, the top (glass) and the rear (substrate: made of a 0.5 mm thick Tedlar: polyvinyl fluoride) rough surfaces of the PV module. The main requirements of both the glass and the encapsulant are stability at elevated temperatures and high UV exposure, low thermal resistivity and optical transparency for the incident radiation to reach the cell.

Despite the high optical transparency of both glass and EVA, inevitably the solar absorption spectrum of the encapsulated solar cell [structure shown in Fig. 1(a)] changes relative to the bare cell, leading to unwanted absorption losses, as shown in Fig. 1(b), where the absorption for a bare cell (red line), an encapsulated cell [15] (green line) and a single 0.46 mm EVA wafer [23] (purple line) is shown. It is clear that EVA strongly absorbs UV radiation ($\sim$< 0.375 μm) reducing thus the available photo-carriers reaching the cell at this regime, while for the wavelength range within the absorption band of silicon (indirect bandgap of $\sim$1.107 μm) the absorption is slightly reduced mainly due to the reflection ($\sim$0.04) introduced from the top surface of the glass. Moreover, unexploitable sub-bandgap absorption, beyond 1.107 μm, up to 4 μm, is still very high, for both the bare and the encapsulated cell, despite that intrinsic silicon does not absorb in this regime. The reason is the non-zero absorption from the highly doped silicon, the metal contacts, the EVA and the thin antireflection layers (usually made of SiN or SiO_2) usually placed on top of silicon, together with the light-trapping effect [12,15]. Consequently, sub-bandgap and UV radiation (of intensity $\sim$150 W/m^2 according to our simulations) not only remains unexploited but also dissipates into heat, which further reduces the efficiency of the solar cell.

In the mid-IR/thermal wavelength range (4-33 μm), the emissivity spectrum of the encapsulated solar cell is mainly determined by the 3.2 mm thick top glass layer. This emissivity is shown in Fig. 1(c), for two cases: for the encapsulated IBC cell (green line) and for a flat fused quartz (blue line) with permittivity data as given by Palik [24]. We see that both cases exhibit strong phonon-polariton resonances at $\sim$9 μm and $\sim$21 μm that allow to achieve relatively strong absorptivity/emissivity in the thermal wavelength range of 7-27 μm. On the other hand, nearby the wavelengths of the phonon-polariton resonances (in the ranges of 8-13 μm and 19-30 μm) there is a strong impedance mismatch between glass and air leading to large reflectivity, associated with dips in absorptivity/emissivity. These emissivity dips coincide with the transparency window of the atmosphere [see Fig. 1(c)], and as a result they lead to reduction of the cooling capability of the system. Therefore, eliminating them is of high importance and has been extensively studied nowadays.

Comparing the two cases of Fig. 1(c_ considering that the encapsulated cell emissivity comes almost exclusively from its top glass layer, we see that the emissivity of the typical PV glass is slightly enhanced compared to that of quartz. In the present study though we utilize the fused quartz as the conventional cooler of the system. The reason is that for the quartz there are available material's permittivity data [24] allowing for both broadband spectral (4-33 μm) and polar/angular emissivity simulations (0-85°) which are both critical for the accurate evaluation of the performance of realistic photonic coolers.

3. Electrical-thermal modeling

Crystalline silicon-based solar cells are basically p-n-homojunction diodes, that is a junction of a n-type and p-type doped silicon which possess an excess of free electrons and holes in their carrier concentrations respectively. The forces acting on the electron and hole carriers to produce an electric current are the gradients introduced by the quasi-Fermi energy level splitting (qV) in both the n- and p-type material [25] under steady-state non-equilibrium illuminated conditions, since the free electron (n) and hole (p) carrier concentrations strongly depend upon illumination. Detailed balance method described by Shockley and Queisser [1] relates the current density, J [in A/m^2], in ideal (and electrically homogeneous) solar cells to the output voltage, V [in V], by

balancing the particles entering and exiting the device. To this extent, the limiting efficiency of such solar cells is due to the balancing of the number of photons absorbed by the solar cell with the number of carriers exiting the cell either to produce electrical power or to result to emission through radiative recombination of electron-hole pairs. In the present work, besides radiative recombination we further take into consideration the only fundamental nonradiative loss mechanism in mono-crystalline silicon (since for mono-crystalline silicon we assume that there are no defects in the crystalline structure), the Auger recombination. Following Shockley's and Queisser's detailed balance method, the current density obtained in an electrically homogeneous mono-crystalline silicon-based solar cell under illumination can be calculated by

$$J(V, T) = J_0(T) \left(e^{\frac{qV}{k_B T}} - 1 \right) + J_A(V, T) - J_{SC}, \tag{1}$$

where q is the elementary charge of an electron [in C], k_B is Boltzmann's constant [in eV/K], T is the operating temperature [in K] and J_A is the nonradiative recombination current density due to Auger recombination. The term

$$J_{SC} = q \int_{0.28}^{1.107} a_{cell}(\lambda) \Phi_{AM1.5G}(\lambda) d\lambda, \tag{2}$$

is the current density flowing at short-circuit conditions under the illumination of the sun. $\Phi_{AM1.5G}$ is the photon flux density [in photons·m^{-2}·s^{-1}·nm^{-1}] of the "AM 1.5G" standard sunlight spectrum [26] reaching the Earth's surface, which is universal when characterizing solar cells. This term is simplified to equal the photocurrent since in Eq. (2) the external quantum efficiency (EQE) of the solar cell (i.e., number of charge carriers collected versus the number of incident photons) is replaced by its absorptivity, α_{cell}, owing to the near-unity internal quantum efficiency (IQE) (i.e., number of charge carriers collected versus the number of incident photons absorbed) in mono-crystalline silicon-based solar cells [27]. The first term in Eq. (1) represents the voltage-dependent radiative recombination current density in the dark. It is a product of the energy distribution of carriers, at a specific operating temperature of the solar cell, that have enough energy to flow through the junction, in the opposite direction from the photogenerated current, and recombine [25]. The energy distribution of carriers and consequently the dark current density follow the Fermi statistics, which, if the Fermi level is lying within the band gap (as in our case), corresponds to Maxwell-Boltzmann statistics. The term qV characterizes the quasi-Fermi energy level splitting, i.e. the difference in the quasi-Fermi levels of electrons and holes (the term "quasi" is due to the non-equilibrium (i.e. under-solar-illumination) steady state). Lastly, J_0 is the saturation radiative current density which is independent of bias and it is determined by the thermal excitation level of carriers quantified by the temperature-dependent blackbody (BB) spectrum (Φ_{BB}, see Eq. 8):

$$J_0(T) = q \int_{0.28}^{1.107} a_{cell}(\lambda) \Phi_{BB}(T, \lambda) d\lambda, \tag{3}$$

The Auger recombination rate, which is specific to the chosen semiconductor material, under Boltzmann's approximation and assuming that $n = p$ and $np >> n_i^2$, is given by [28,29]

$$J_A(V, T) = q \cdot 2A_r(T) \cdot n_i^3(T) \cdot e^{\left(\frac{3qV}{2k_B T} \right)} \cdot W, \tag{4}$$

where W is the thickness of the silicon layer. The temperature-dependent Auger coefficient, $A_r(T)$, is extracted from Ref. [30] and it describes solar cells with lowly doped silicon base, such as today's optimum crystalline silicon solar cells [31,32]. The temperature-dependent intrinsic carrier concentration, $n_i(T)$, is the commonly accepted value by Refs. [33,34]. As

proven in Ref. [34] at 300 K, at lower doping densities ($<10^{16}$ cm^{-3}, like IBC cells and relevant for the optimum crystalline silicon solar cell) and low carrier injection levels (as in solar cells of typical resistivities), the impact of silicon bandgap narrowing with temperature-increase is not significant; hence it is neglected in our study.

Equation (1) assumes that the dark current density remains the same during illuminated conditions and the net current density is shifted in negative current direction by the photocurrent J_{SC} (that flows in the opposite direction from the dark current) which at least for silicon-based solar cells is independent of the bias [35]. In such cases, the superposition [see Eq. (1)] between the dark and illuminated JV characteristics of a diode is valid. The efficiency, η, of the solar cell is given by

$$\eta = \frac{P_{ele,\max}}{P_{inc}} = \frac{J_{SC}V_{OC}FF}{P_{inc}} = \frac{J_{mp}V_{mp}}{P_{inc}}, \tag{5}$$

where $P_{ele,\,\max} = \max(-JV) = J_{mp}V_{mp}$ is the electrical power density output of a solar cell operating at the maximum power point [36], P_{inc} is the incident power density of the incoming sun radiation and $FF = J_{mp}V_{mp} / J_{SC}V_{OC}$ is the fill factor. The term V_{OC} is the maximum voltage, usually referred as the open-circuit voltage, and results from Eq. (1) by setting the total current $J = 0$ and solving for V.

As discussed above, the limiting efficiency of a solar cell depends upon balancing of particles entering and exiting the device for a specific operating temperature of the system. More specifically, assuming only radiative recombination, if the cell operates at high temperature (thus the current J_0 becomes higher) the quasi-Fermi energy level splitting (qV) must be reduced to maintain a balance between the number of absorbed photons and the number of the emitted photons [37]. This results to lower V_{OC} and V_{mp} and lower efficiencies. Regarding the nonradiative (Auger) recombination process, J_A scales with the intrinsic carrier concentration cubed [see Eq. (4)]. Therefore, at elevated temperatures the Auger recombination rate is higher due to the increased thermally generated carrier concentrations.

It is important to note here that two of the main assumptions of our theoretical modeling are that we neglect the effect of how efficiently the contacts collect the photo-generated carriers and the impact of the PV defects. Such assumptions are quite valid for calculating the absolute efficiency of mono-crystalline silicon-based solar cells since their internal quantum efficiency is near-unity [27]. Primarily, since we are mostly interested in the efficiency changes owing to the operating temperature variations, studies have shown that the decrease of η with increasing temperature is mainly controlled by the reduction of V_{OC} with T (for relatively highly-efficient cells the V_{OC} change usually constitutes the 80 to 90% of the η change) [38,39]. Therefore, the temperature impact on both the contact resistance and J_{SC} is neglected in the present study, thus leaving the efficiency dependence with temperature to be mainly controlled by the intrinsic (radiative, non-radiative Auger mechanisms) material properties of the semiconductor of the solar cell. Regarding the impact of the PV defects, the better the surface passivation of the solar cell, the stronger the influence of recombination in the bulk material, and in case of low bulk defect concentrations [high Shockley-Read-Hall (SRH) life-times] the Auger recombination becomes dominant [32,40]. Hence, in highly-efficient cells with minimum power-temperature coefficients the Auger recombination mechanism [20] prevails over the other possible non-radiative recombination mechanisms, justifying the assumptions of our modelling.

To take into consideration the effect of heating in solar cells, and thus to be able to calculate the extracted electrical power or efficiency in respect to the operating temperature at typical outdoor conditions, we perform a thermal analysis. The steady-state temperature or the operating temperature of the cell of a photovoltaic module can be accurately described by treating the PV as a uniform device by using appropriately combined conduction-convection heat transfer coefficients. A thermal analysis for the PV can thus be performed by balancing the total power into and out of the device following Planck's blackbody formalism and Kirchhoff's law, i.e.,

absorptivity equals emissivity. This strategy (PRC: passive radiative cooling strategy) was firstly proposed by Fan [11,41] for calculating the radiative cooling of solar absorbers and has been shown to exhibit highly accurate results [12]. According to Fan, when a structure is exposed to a daylight sky, it is subject to both solar irradiance and atmospheric thermal radiation (corresponding to ambient air temperature T_{amb}). In our case [structure of Fig. 1(a)], the net cooling power, $P_{net,cool}$, of a PV can be determined by summing the total power into and out of the device [37]:

$$P_{net,cool}(V,T) = P_{rad,cooler}(T) - P_{atm}(T_{amb}) + P_{cond+conv}(T_{amb},T) - P_{solar,heat}(V,T), \quad (6)$$

where $P_{\text{rad,cooler}}$ is the power density radiated by the radiative cooler (see Eq. 10), i.e. the top glass layer, and P_{atm} is the power density absorbed by the cooler from the atmospheric emission that takes into consideration the atmospheric transparency window [42] [see Eq. (11)]. $P_{\text{cond,conv}} = h_c(T - T_{\text{amb}})$ is the power density loss (since in our case $T > T_{\text{amb}}$) due to convection and conduction, where $h_c = h_{\text{cond}} + h_{\text{conv}}$ is a combined nonradiative heat transfer coefficient that captures the collective effect of conductive and convective heating owing to the contact of the cell with external surfaces and the air adjacent to the top radiative cooler. The last term, $P_{\text{solar,heat}}$, is the absorbed solar power density that dissipates into heat which incorporates the electrical part and formulates as follows:

$$P_{solar,heat}(V,T) = P_{sun} - P_{ele,\max}(V,T) - P_{rad,cell}(V,T), \quad (7)$$

In Eq. (7) P_{sun} is the total solar absorption power density [see Eq. (12)], and $P_{\text{rad,cell}}$ is the power density radiated by the solar cell also known as the non-thermal radiation (emitted through electron-hole recombination, as a consequence of the bandgap of the semiconductor material [43] – see Eq. 14). Consequently, we notice that both the quasi-Fermi energy level splitting (qV) and the operating temperature characterize the emission. In this way, the electrical power of a PV exposed to the outside at a corresponding operating temperature, defined as the steady state temperature or operating temperature, is self-consistently determined by obtaining the solution of Eq. (6) with $P_{\text{net,cool}} = 0$ for a solar cell operating at the maximum power point ($V = V_{\text{mp}}$).

In the current work we consider a conventional radiative cooler (glass slab of thickness 3.2 mm and material parameters given by Palik [24]) with an absorptivity/emissivity, $\varepsilon(\lambda,\theta)$, that is calculated by performing full-wave electromagnetic simulations for wavelengths from 4 up to 33 μm with a 5° angular resolution using the commercially available software CST Microwave Studio. Moreover, we determine the absorptivity/emissivity of the cell $\varepsilon_{\text{Si}}(\lambda)$ by the data deduced from Fig. 1(b) from Refs. [15,23].

4. Physical mechanisms, requirements and potential for cooling radiatively photovoltaics

To evaluate/validate our approach initially we calculated the efficiency and the open circuit voltage changes with respect to the operating temperature variations assuming the aforementioned theoretical model for the crystalline silicon-based PV. Then, we compared our calculated power-temperature and voltage-temperature coefficients (i.e., the slopes of the $P_{\text{ele,max}}$-T, V_{OC}-T curves) with those of commercial PVs measured and provided by the manufacturers (the slopes of the $P_{\text{ele,max}}$-T, V_{OC}-T curves are normalized at % compared to a PV operating at Standard Test Conditions (STC) [i.e., 1000 W/m^2 irradiance, AM 1.5G, T_{cell}=298.15K]). In particular, we calculated, for our theoretical PV (with silicon data obtained from Refs. [30,33], see Section 3), a constant power-temperature coefficient equal to -0.293%/K and a voltage-temperature coefficient equal to -0.244%/K, confirming that the efficiency changes with temperature are linear. The above values of power-temperature and voltage-temperature coefficients, despite being lower compared to the mainstream silicon-based modules (with power-temperature coefficients around

-0.45%/K to -0.40%/K), they match the data of well-optimized and highly-efficient PVs, such as the SunPower's Maxeon Gen III IBC solar cells [44,45]. For highly efficient PVs our calculations showed that the efficiency changes are mainly controlled by the voltage changes with temperature; this is a consequence of the increased carrier concentrations at elevated temperatures and hence increased nonradiative recombination in the bulk [4,32], further supporting the validity of our assumptions.

In general, the minimum power-temperature coefficients imply that only the intrinsic radiative and the Auger recombination mechanisms [20] are considerable. Indicatively, assuming only radiative recombination, the power-temperature and voltage-temperature coefficients are reduced almost down to the half (-0.168%/K, -0.117%/K), implying a significant underestimation of the efficiency increase related to the temperature reduction that could be provided by a radiative cooler. The very good agreement of our theoretical calculations with the experimental data of Refs. [44,45] provided by the PV manufacturers allowed us to continue with the examination of the radiative cooling impact on the efficiency assuming optimized PVs which operate outdoors.

After determining the dependence of the PV efficiency on temperature, we need next to relate the temperature with the power that either cools or heats the solar cell. Such a relation provides an effective way to evaluate the temperature reduction provided by different cooling approaches or approaches that reduce heat generation. The impact of a certain amount of heat extracted or added to a system on system's temperature depends upon the slope of the net cooling power – temperature curve [$P_{net,cool}$ $(T) = P_{rad,cooler}$ (T) - P_{atm} $(T_{amb}) + P_{cond+conv}$ $(T_{amb}, T) + P_{solar,heat}$, see Eq. (6)] (for different weather conditions). As an example, in our case we fix the solar heating power, $P_{solar,heat}$ in Eq. (6), to be 620 W/m^2, corresponding approximately to the expected heat output of a crystalline solar cell under peak unconcentrated solar irradiance (1000 W/m^2). The steady-state is at $P_{net,cool}(T) = 0$. The weather conditions are included in the model by considering different combined conduction-convection nonradiative heat transfer coefficients, h_c, in the $P_{cond+conv}$ term of Eq. (6) and different T_{amb} in the P_{atm} term. For example, in windy conditions h_c increases. In Fig. 2, we present the net cooling power for $T_{amb}=300$ K with respect to the cooler's temperature T for two types of coolers, (i) the flat fused quartz thermal emitter (solid lines) and (ii) assuming a theoretical ideal thermal emitter, i.e., one exhibiting maximum emissivity along the entire thermal wavelength (4-33 μm) range for all angles of incidence (dashed lines).

As can be seen in Fig. 2, at steady state [$P_{net,cool}$ $(T) = 0$] (see horizontal black line) for typical outdoor conditions ($h_c \geq 12$ W/m^2/K) we come up with typical PV operating temperatures (~325 K) under peak solar irradiance. Moreover, the net cooling power has a more linear-like response in the typical operating temperature range of PVs (310 K – 345 K), especially for higher values of h_c. Thus, a certain amount of power (either extracted or added to the system) has a certain impact on temperature (reduction or increase) which depends upon the magnitude of the slope of the net cooling power-T curve for each line/cooling condition. Accordingly, when we reflect the parasitic UV and sub-bandgap absorbed radiation in PVs, the impact of the reflected power on the operating temperature reduction depends upon the slope/derivative of the net cooling power -T curve corresponding to each cooling condition (i.e., for each h_c and for each cooler). Lower derivatives indicate higher temperature reduction for the same power reflected. These conclusions are consistent with previous results [18,19,20]. In Ref. [20] in particular, it was demonstrated that the impact of lowering the thermal load is the largest when the convective cooling is the weakest (i.e. for the smallest h_c) with a very small dependence on outdoor temperature (not shown here). Accordingly, we can determine coefficients related to the extracted power needed for 1 K temperature reduction for each weather condition. Assuming realistic weather conditions (i.e., $T_{amb}=300$ K, $h_c \sim 12$ W/m^2), the net cooling power -T coefficient (slope) equals to 17.9 W/m^2/K or 19.3 W/m^2/K for the conventional or the ideal thermal emitter respectively. The net cooling power-T linear-like response further indicates that the power
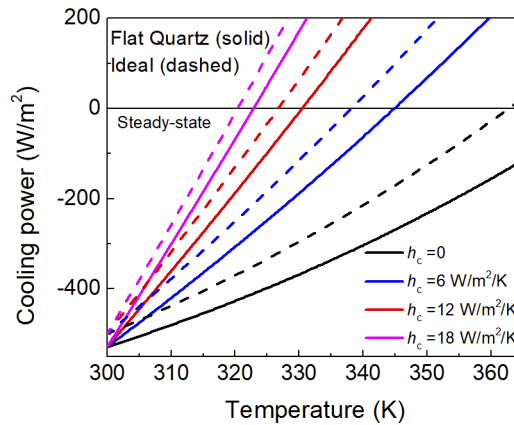
Fig. 2. Net cooling power vs. cooler's temperature T assuming a fixed solar heating power, $P_{solar,heat} = 620 \, \mathrm{W/m^2}$, emulating that of a c-Si PV, for $T_{amb} = 300 \, \mathrm{K}$ and for different combined conduction-convection nonradiative heat transfer coefficients, h_c, for a flat fused quartz thermal emitter (solid lines) and an ideal thermal emitter, i.e., exhibiting maximum emissivity along the entire thermal wavelength range (4-33 μm) for all angles of incidence (dashed lines). The steady-state is at $[P_{net,cool}(T) = 0]$ (horizontal black line).

variations at the system play the most crucial role for the temperature variation rather than the exact initial value of its heating power. This is not as accurate for solar cells operating at low-wind conditions, where the net cooling power-T curve does not approach a linear-like response.

From Fig. 2, it is also clear that when we alter the cooling system, that is when we optimize the conventional thermal emitter towards the ideal, the net cooling power increases and so does the slope, which is evident from the power difference between the solid and the dashed curves. Increased net cooling power results to an "in" and "out" power balance $[P_{net,cool}(T) = 0]$ at lower temperatures [12,16,20] (see Fig. 2). Indicatively, for $h_c = 12 \, \mathrm{W/m^2}$, the temperature reduced by ~4 K when the ideal cooler was utilized instead of the flat quartz. This justifies the increased interest in optimizing radiative-coolers over the recent years. However, passive radiative cooling (PRC) impact, that is the steady-state temperature difference between the conventional and the ideal thermal emitter, decreases as h_c increases, as can be seen in Fig. 2 by comparing the solid lines versus the dashed curves (at steady-state, see horizontal black line in Fig. 2), in agreement also with Ref. [20], and further weakens with increasing outdoor temperature, T_{amb}, (see Ref. [20]). Interestingly though, PRC impact is still prominent even for high h_c values (>12 W/m^2/K). As highlighted also in [20], a gain will always be observed when adding radiative cooling, in particular in conditions where convective cooling tends to become inefficient.

We notice in Fig. 2 two crossing points of the lines concerning the different cooling conditions (different h_c), at $T = T_{amb} = 300 \, \mathrm{K}$, one for each of the two cooling systems. The meaning of these crossing points is that for $T = T_{amb} = 300 \, \mathrm{K}$ the nonradiative heat transfer, i.e., due to convection [third term in right-hand side of Eq. (6)] is zero due to the nonradiative thermal equilibrium [11,46]. At $T = T_{amb} = 300 \, \mathrm{K}$, the ideal cooler (dashed lines in Fig. 2) provides a higher net cooling power (~31 W/m^2) compared to the flat quartz (solid lines in Fig. 2) owing to the enhanced emission at the universe (through the atmospheric transparency window) [11,46] of a much lower temperature (~3 K) than that of the atmosphere (~300 K).

In Fig. 3 we present the impact of different photonic approaches (among the ones discussed in the Introduction) on both the temperature reduction [Fig. 3(a)] and the efficiency enhancement [Fig. 3(b)] of the PV discussed in Sections 2 and 3, by employing the coupled thermal-electrical modeling proposed in this work (comparing to the same PV with no photonic approach

implemented). We note that the absorptivity/reflectivity properties of the PV are those discussed in Section 2 and the electrical properties are those discussed in Section 3, applying mostly to optimized mono-crystalline silicon IBC PVs (for application to other types of commercial silicon-based photovoltaic cells different radiative and electrical properties might be chosen). The approaches presented include reflection of parasitic UV radiation (*UV* – black lines), reflection of the sub-bandgap radiation (*Sbg* – magenta lines), implementation of an ideal mid-IR thermal emitter (*Ideal* – green lines), and combinations of all the above. In the combined case of the reflection of both UV and sub-bandgap radiation and the additional implementation of the ideal thermal emitter (purple lines) the effect of changing the T_{amb} (triangles) and the silicon thickness (*W*) (circles) is also demonstrated. The cases with climates with very weak winds or assuming protective windshields are found in the regime lower than $h_c = 10.6$ W/m^2/K which in Figs. 3(a) and 3(b) are at the left of the corresponding vertical lines. Cases with stronger winds are found in the right of the vertical $h_c = 10.6$ W/m^2/K lines.
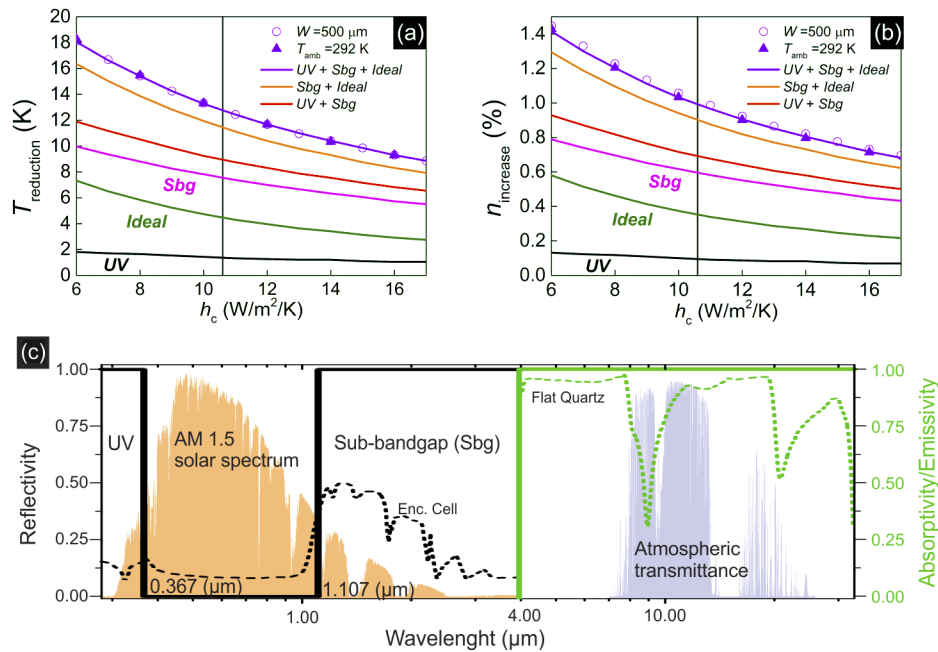

Fig. 3. (a) PV temperature, *T*, reduction and (b) efficiency, η, increase associated to different radiative approaches with respect to the combined conduction-convection nonradiative heat transfer coefficient h_c (the reduction and increase are relative to the PV without any implemented cooling approach). Black lines correspond to the reflection of parasitic UV assuming an IQE = 1, magenta lines correspond to the reflection of the sub-bandgap radiation, green lines correspond to the implementation of an ideal mid-IR thermal emitter, i.e., exhibits maximum emissivity along the entire thermal wavelength range (4-33 μm) for all angles of incidence, red lines correspond to the reflection of both UV and sub-bandgap radiation, orange lines correspond to the reflection of sub-bandgap radiation and the additional implementation of the ideal thermal emitter. Purple lines correspond to the reflection of both UV and sub-bandgap radiation and the additional implementation of the ideal thermal emitter. Triangles show the effect of the last approach for different T_{amb} (i.e. 292 K instead of 300 K) and circles for different silicon thickness (*W*) (i.e. 500 μm instead of 250 μm). Cases at the left of the vertical line correspond to climates with very weak winds or assuming protective windshields. (c) Optimum reflectivity and emissivity spectrum (solid lines) for a crystalline-silicon PV in comparison with PV's reflectivity and flat quartz's emissivity (dashed lines).

For calculating the results related to the reflection of the UV radiation, we introduced an algorithm in the theoretical modeling. This algorithm gradually generates a total reflection (that equals unity) from wavelength equal to 0.28 µm (highest thermalization losses) till the optimum wavelength, with a wavelength step of 0.0003 µm. In this way, we examine the relative contribution of the UV spectrum on the efficiency of a PV, considering also that the thermalization process at that regime is quite prominent as the excess energy of photons relative to the bandgap of the semiconductor is high, in addition to the high parasitic absorption from EVA. We found that the reflection of the UV radiation led to an (absolute) PV efficiency increase (by ~0.1%) rather than a decrease, despite the reflection of potential currents. In other words, the negative effects of EVA absorption and thermalization losses seem to overcompensate the positive effect of the additional potential currents generated by the UV. For all weather conditions the optimum reflection wavelength range was found from 0.28 µm to 0.367 µm (EVA parasitic absorption nearly 0.85 at 0.367 µm). As a result, as concluded by our analysis and can be seen in Fig. 3, for PVs with UV-absorbing encapsulants the cost of the existing techniques for screening harmful [47] UV radiation and surface passivation techniques [48] (due to defects at the front surface of the cell acting as recombination traps) could be reduced considerably as well as the aging rate [49] since both an efficiency increase and a temperature reduction can occur despite reflecting incident UV radiation within the absorption band of silicon.

From Figs. 3(a) and 3(b), it is also clear that the most efficient cooling approach in crystalline silicon-based PVs is the reflection of sub-bandgap radiation, due to the relatively high parasitic absorption from the PV module at that regime, consistently with Refs. [18,20]. It should be noted that the choice of a PV architecture has an impact on its radiative properties (absorptivity, reflectivity), as is clearly shown in Refs. [17,19,20]. For example, a higher impact from the reflection of the sub-bandgap radiation could be expected in certain top contact solar cells, where there is additional parasitic absorption from the metallic top contacts (thus higher room for heat elimination) [15] or a lower impact for passivated emitter and rear cells (PERC) [19]. From Figs. 3(a) and 3(b) we note that the cooling impact from the reflection of the sub-bandgap radiation could be more prominent if combined with the reflection of UV radiation. Moreover [see Fig. 3(a)] an ideal thermal emitter provides also a significant temperature reduction (see also Fig. 2). Combining all photonic approaches, a highly-efficient crystalline silicon-based PV can reach ideally a temperature reduction of up to 18 K, corresponding to an ~1.42% overall efficiency increase (compared to the same PV where no any radiative approach has been applied), and up to 12.7 K corresponding to an ~1.0% overall efficiency increase assuming more realistic operating conditions ($h_c \geq 10.6$ W/m^2/K). In the solar cell industry, such an improvement is expected to lead to an increased lifetime [7] of the solar cell array, more than doubled, and an increased profit. A higher efficiency increase for the same temperature reduction can be expected in mainstream PVs with higher electrical-power-temperature coefficients (common value of -0.45%/K). Interestingly, higher temperature reductions, due to radiative cooling, has been shown in concentrated PV systems by using a conducting surface area larger than the cell itself [50].

Operating temperature reduction remains almost the same if assuming an 8 K lower ambient temperature as seen in Fig. 3(a). Interestingly, although for T_{amb}=292 K the PV operates at ~7 K lower temperature than for T_{amb}=300 K, the temperature reduction offered by the cooler does not decline. These results suggest that the radiative cooling strategy could be effectively utilized no matter the climate. Moreover, assuming a much thicker silicon layer in the PV, i.e. of $W = 500$ µm, and assuming the same absorptivity and reflectivity of the cell (so as to highlight on the intrinsic quantum yield dependence with temperature and cell' thickness), the operating temperature reduction remained almost the same. However, the efficiency increase for the case of a PV with $W = 500$ µm is slightly higher (up to 0.032%), compared to that of $W = 250$ µm, due to the alteration of the voltage- (-0.253%/K) and power-temperature (-0.303%/K) coefficients of the device arising from the nonradiative recombination rate dependence on W [see Eq. (4)].

Consequently, we conclude that the radiative cooling of PVs is a very robust strategy to increase their efficiency, in respect with the varying operating conditions and the various characteristics that are met in commercial PVs.

Treating the PV as a quantum device instead of a solar absorber, i.e. taking into account also the electrical power generated by the incoming radiation besides the heating effect of that radiation [see Eq. (7)], we noticed up to ∼1.1K smaller temperature reduction (corresponding to a ∼0.32% lower power output) when an ideal thermal emitter was applied instead of the conventional thermal emitter. The reason was the lower amount of solar heating power, due to the electrical power output from the PV, which led the device to operate at lower temperatures, where the PRC impact is lower. Thus, since the optimization of the thermal emitter affects the nonradiative recombination rate only through the temperature, the efficiency increase in a PV due to the temperature reduction provided by the thermal emitter can be described with an error up to 1.1K by employing the PRC modeling (treating the PV as a solar absorber) and the power-temperature and voltage-temperature coefficients of the PV manufacturers. On the other hand, optimizing a radiative cooler unavoidably results to changes in the optical response of the system; for example, it may affect greatly the transparency from the top surface of the PV and hence, the J_{SC} and the efficiency. Therefore, as it will be shown and in the next section, when utilizing a radiative cooler in a PV device, it is also necessary to weigh the interplay between the requirements for transparency in the optical spectrum and the enhanced, broadband thermal emission in mid-IR, and the way that they affect the cooler's reliability and fabrication cost.

5. Towards realistic implementation

In this last section, we apply the theory presented in the previous sections in the case of realistic photonic coolers proposed in the literature to evaluate and examine how far the current realistic implementations have come towards the maximum potential of the radiative thermal management in commercial solar cells, i.e. how close they are to the ideal implementation of all the cooling approaches shown in Fig. 3. Several studies [12–16] utilizing photonic radiative coolers for solar cells have emerged over recent years. In our study we pick two of them to highlight and distinguish the cooling gain that arises in one case mostly by the photon management at the optical regime (Wei Li et al. [15] in 2017) and in the other case at the mid-IR (Linxiao Zhu et al. [12] in 2015). Zhu et al. [12] exploited a 2D photonic crystal (PC) on top of a solar absorber (with a structure that emulated the behavior of a real silicon solar cell) which consisted of periodically placed air holes (∼10 μm depth, ∼6 μm periodicity) of non-vertical sidewalls in silica [see bottom structure of Fig. 4(a)]. The nonvertical sidewalls of the holes resulted in a gradual refractive index change which provided effective impedance matching between silica and air over a broad range of thermal wavelengths [see Fig. 4(c)] that persisted even for larger angles of incidence [see Fig. 4(d)]. Moreover, this visibly transparent thermal black-body led to the increase of the absorbed solar power in silicon due mainly to the enhanced transparency from the top surface [see Fig. 4(b)]. Later, Wei Li et al. [15] proposed a 1D photonic crystal consisting of 45 alternate Al_2O_3, SiN, SiO_2, TiO_2 thin-film layers that could be implemented as a retrofit to current photovoltaic modules [see top structure of Fig. 4(a)]. This photonic coating layer was designed to be placed on top of a PV and simultaneously reflect part of the solar spectrum that does not contribute to the photocurrent, i.e., the UV, sub-bandgap parasitic absorption, and further enhance the beneficial optical absorption [see Fig. 4(b)] and the thermal radiation in the mid-IR [see Figs. 4(c), 4(d)].

As can be seen in Figs. 4(c), 4(d), the 1D PC exploits lower emissivity than the 2D PC at the thermal mid-IR wavelength range for all polar angles. On the other hand, the 1D PC provides a direct heat extraction, calculated as ∼92 W/m^2 out of ∼150 W/m^2, through the reflection of the parasitic UV and sub-bandgap solar absorption in optical [see Fig. 4(b)]. Using
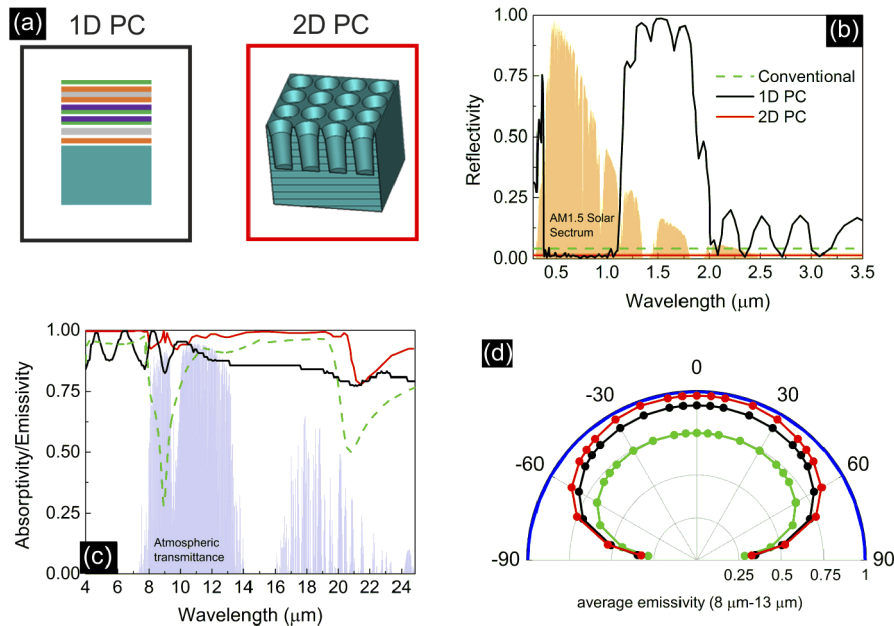
Fig. 4. (a) Illustrations of a 1D photonic crystal consisting of alternate Al_2O_3, SiN, SiO_2, TiO_2 thin-film layers (top structure, in a black rectangle) and a 2D photonic crystal of non-vertical sidewalls in silica (bottom structure, in a red rectangle). (b) Reflectivity spectra of the 1D (black line) and 2D (red line) photonic crystals in comparison with the conventional case (flat fused quartz - green line) and (c) their emissivity spectra over the thermal wavelength range in mid-IR. Data are extracted from Refs. [12,15,24]. (d) Average emissivity between 8 and 13 μm (the atmospheric transparency window) plotted as a function of polar angle of incidence, for the 1D (black line) and 2D (red line) photonic crystal in comparison with the conventional (green line) and the ideal case, i.e., an overall ideal photonic cooler and not just an ideal thermal emitter (blue line).

the cooling-power-temperature coefficients discussed in Section 4, for the 1D PC case, the temperature reduction is expected to equal ~4.7 K for the ~92 W/m² of reduced heat generation.

The roles of the 1D, 2D PC as radiative coolers in silicon PV modules were then investigated through current-voltage (J–V) calculations [see Eqs. (1), (3), (4)], and are shown in Fig. 5. In particular, we present the recombination current density [first two terms in the r.h.s, of Eq.. (1)]), Fig. 5(a), and the output current density, Fig. 5(b), for an operating temperature equal to the steady-state temperature arising by setting $P_{net,cool}(V, T) = 0$ in Eq. (6), assuming T_{amb}=298 K and a nonradiative heat transfer coefficient equal to 13.7 W/m²/K to mimic typical outdoor conditions. The corresponding output electrical power and the steady-state temperature are presented in Figs. 5(c) and Fig. 5(d) respectively. Notice that as the electrical power increases the temperature drops due to heating reduction. The lowest operating temperature occurs at the maximum power point of the PV. The results are also compared with the ones that could be achieved ideally, that is assuming optimum performance in mid-IR and optimum reflection in optical, i.e., assuming an overall ideal photonic cooler and not just an ideal thermal emitter.

In Fig. 5(b) we observe that the useful current density increases for the ideal case and the photonic crystal radiative coolers cases in the voltage range of 0.55-0.71 V. This is also related to the enhanced short-circuit current density as calculated from Eq. (2) which is increased from 396.4 A/m² to 406.9 A/m². [The short-circuit current density is equal to the current density at voltage = 0 V, not shown in Fig. 5(b).] This ~2.6% short-circuit current density increase is due to
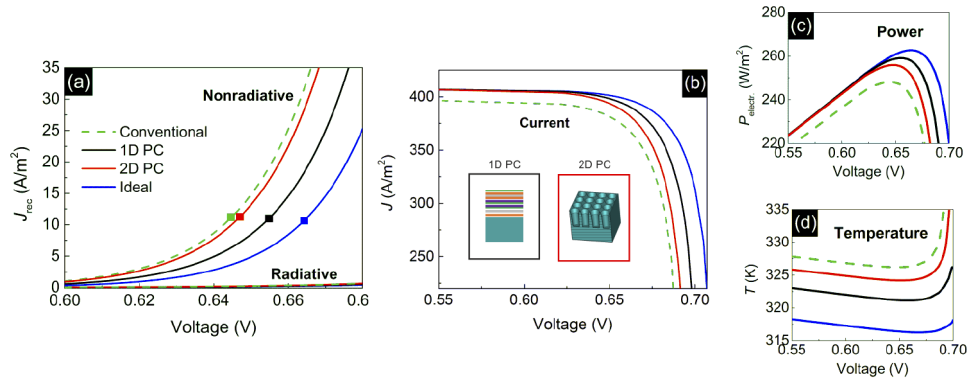
Fig. 5. (a) Nonradiative and radiative recombination current density (J_{rec}) vs. applied voltage and the (b) current density vs. applied voltage of two PVs that incorporate a 1D photonic crystal (see top structure of Fig. 4(a) and a 2D photonic crystal (see bottom structure of Fig. 4(a) in comparison with the conventional PV (green line) and the ideal case assuming an overall ideal photonic cooler and not just an ideal thermal emitter (blue line). The squares in (a) denote the nonradiative (Auger) recombination current density at the maximum operating power point, V_{mp}, of the solar cell. (c) Electrical power output and the (d) operating temperature of the device vs. applied voltage for each case. Both (c) and (d) are calculated for the steady-state $P_{net,cool}(V, T) = 0$.

the increased top surface transmissivity in the wavelength range within the absorptive band of silicon, provided from both photonic structures relative to the conventional flat glass. Moreover, despite the increased solar absorption (and hence the associated increased thermalization losses that resulted to higher heat dissipation in the structure), at the steady-state ($P_{net,cool}(V, T) = 0$) the cooling properties of the 1D and 2D PCs result in operating temperature reduction compared to the conventional photovoltaic module. In particular, as seen in Fig. 5(d), the temperature reduction at the maximum operating point of the PV [Vs marked with squares in Fig. 5(a)] is equal to 5.1K for the 1D PC and 1.4K for the 2D (ideally: ~10K). This results in the increase of the open-circuit voltage, V_{OC}, by 1.4% and 0.42% respectively (ideally: ~2.6%).

The reason behind the V_{OC} enhancement in all cases is the reduced nonradiative (Auger) recombination arising by the temperature reduction provided by the coolers. More specifically, as shown in Fig. 5(a), the nonradiative recombination current density decreases when we optimize the cooling capability of the PV by employing the 2D, 1D PCs and the ideal photonic cooler. The reduced operating temperature provided by the coolers results to increase of the maximum power point voltages V_{mp} [extracted from Fig. 5(c)] as we optimize the cooler from the conventional to the ideal case [see Fig. 5(a)]. Moreover, one can see that the impact of the radiative recombination current density is much lower than the non-radiative in all cases consistent with Refs. [3,32], further validating our assumptions in Section 3. Results shown in Figs. 5(a) and 5(b) indicate improved dark current characteristics of the diode (the dark current is calculated from Eq. (1) when the $J_{SC}=0$) that were achieved by the utilization of the photonic coolers since V_{OC} increases as the saturation recombination current density decreases. Additionally, we note here, that with the increase of J_{SC} the thermalization losses process increases too which slightly lowers V_{mp} in all cases. However, the impact of this lowering on the efficiency was much smaller compared to the J_{SC} contribution itself. Moreover, the fill factor FF is also improved by 0.03%, 0.3%, 0.6% for the 2D, 1D PCs and the ideal case respectively. Eventually, the conversion efficiency is further increased, due to the J_{SC} increase and the V_{OC} increase, and hence the improved dark characteristics of the diode. In particular, as also seen at the maximum power points of Fig. 5(c), the conversion efficiency is increased by 3.1% in relative terms for the 2D PC case and by 4.3%

for the 1D PC case, leading to higher overall efficiencies by 0.77% and 1.08% respectively with respect to the conventional PV; these values are quite close to the ideal case, calculated at ~+1.44%. Interestingly, aiming primarily for an enhanced thermal-emitter-cooler compared to an optical-reflector-cooler leads to an ~0.31% overall efficiency decrease.

6.   Conclusions

In this work we examined and discussed the physical mechanisms and requirements for cooling radiatively selected state of the art mono-crystalline silicon-based PVs. Besides radiative cooling, common photonic strategies for reducing heat generation within the PV cell, such as ultraviolet and sub-bandgap reflection, were also examined. This was done by employing an electrical-thermal co-model which takes into account all the major intrinsic processes affected by the temperature variation in a PV device. The accuracy and applicability of our model was tested through comparison with experimental data provided by PV manufacturers concerning highly-efficient IBC solar cells.

Employing our electrical-thermal model we found that the main reason of the efficiency decrease due to the heating in crystalline silicon-based PVs is the increased nonradiative recombination at elevated temperatures, which reduces the open-circuit-, and the maximum-point-voltage, consistently with literature. Examining the relative potential of the different possible photonic approaches for temperature reduction in the PVs under consideration we found that the most efficient approach is the reflection of sub-bandgap radiation, due to the relatively high parasitic absorption from the PV module at that regime. Moreover, our study showed that the reflection of the UV radiation could also lead to decreased PV operating temperature and enhanced efficiency.

Finally, we showed that the photonic approaches for the PV thermal management constitute a quite robust strategy to increase the PV efficiency, in respect to the varying operating conditions and the various characteristics of crystalline silicon-based PVs. Improving radiative cooling by utilizing photonic structures that additionally reduce heat generation (by reflecting, e.g., sub-bandgap and UV) and enhance photocurrent (by enhancing optical absorption) can reduce the PV operating temperature up to ~10K (ideally) and enhance the efficiency up to ~5.8%, compared to PVs with conventional coolers (flat glass).

Appendix

The steady-state temperature or the operating temperature of the cell of a photovoltaic (PV) module can be accurately described by treating the PV as a uniform device by using appropriate combined conduction-convection heat transfer coefficients. A thermal analysis for the PV can thus be performed by balancing the total power into and out the device following Planck's blackbody formalism and Kirchhoff's law, i.e., absorptivity equals emissivity, as is described in Section 3 of the main text.

Following Planck's formulation, the photon flux (Φ_{BB}) and the spectral irradiance (φ_{BB}) of a blackbody at a temperature T can be well accounted by:

$$\Phi_{BB}(T, \lambda) = \left(\frac{2\pi c}{\lambda^4}\right) \cdot \frac{1}{e^{\frac{hc}{\lambda k_B T}} - 1}, \tag{8}$$

$$\varphi_{BB} = \left(\frac{2hc^2}{\lambda^5}\right) \cdot \frac{1}{e^{\frac{hc}{\lambda k_B T}} - 1}, \tag{9}$$

where h is Planck's constant, k_B is Boltzmann's constant, c is the speed of light. The power density (W/m^2) radiated from a surface, in our case from the surface of the cooler, is then given

by

$$P_{rad,cooler}(T) = \int d\Omega \cos\theta \int_0^\infty \varphi_{BB}(T,\lambda)\varepsilon(\lambda,\theta)d\lambda, \tag{10}$$

Here $\int d\Omega = \int_0^{\pi/2} d\theta \sin\theta \int_0^{2\pi} d\varphi$ is the angular integral over a hemisphere, and by using Kirchhoff's radiation law we replace the structure's absorptivity $\alpha(\lambda,\theta)$ by its emissivity $\varepsilon(\lambda,\theta)$. The term

$$P_{atm}(T_{amb}) = \int d\Omega \cos\theta \int_0^\infty \varphi_{BB}(\lambda,T_{amb})a(\lambda,\theta)\varepsilon_{atm}(\lambda,\theta)d\lambda, \tag{11}$$

describes the absorbed by the cooler thermal radiation emitted from the atmosphere, where the angle-dependent emissivity of the atmosphere is given by: $\varepsilon_{atm}(\lambda,\theta) = 1 - t(\lambda)^{1/\cos\theta}$, and $t(\lambda)$ is the atmospheric transmittance in the zenith direction. The term

$$P_{sun} = \int_0^\infty a_{cell}(\lambda,\theta_{sun})\varphi_{AM1.5G}(\lambda)\cos\theta_{sun}d\lambda, \tag{12}$$

is the total solar absorption power density by the cell, where the solar illumination is represented by $\varphi_{AM1.5G}(\lambda)$, the AM1.5 spectrum [26] and $\alpha_{cell}(\lambda)$ is the cell's absorptivity. In Eq. (12) we assume that the structure is facing the sun at a fixed angle θ_{sun}. Thus, the term P_{sun} does not have an angular integral, and the silicon layer's absorptivity $\alpha_{cell}(\lambda,\theta_{sun})$ is represented by its value at θ_{sun}. P_{sun} either dissipates into heat or results to beneficial electrical power (calculated using the method of detailed balance by Shockley and Queisser [1] described in Section 3 of the main text) and emitted power by the cell:

$$P_{rad,cell}(T) = \int d\Omega \cos\theta \int_{0.28}^{1.107} \varphi(\lambda,T,qV_{mp})\varepsilon_{cell}(\lambda)d\lambda, \tag{13}$$

The power density radiated by the surface of the cell over a hemisphere, $P_{rad,cell}(T)$, is also known as the non-thermal radiation emitted by the solar cell due to the consequence of the bandgap of the semiconductor material [43]. Consequently, both the quasi-Fermi energy level splitting (qV), i.e. the difference in the quasi-Fermi levels of electrons and holes (the term "quasi" is due to the non-equilibrium (i.e. under-solar-illumination) steady state), and the operating temperature characterize the emission. Following Wurfel's generalized Planck law [43], the emitted spectral irradiance, φ, under the applied bias voltage V (for $E - qV \gg k_BT$, where E is the energy in eV), is given by:

$$\varphi(V,T,\lambda) = \varphi_{BB}(T,\lambda)e^{\frac{qV}{k_BT}}, \tag{14}$$

In Eq. (13) we assume that the solar cell is operating at the maximum power point ($V = V_{mp}$). Finally, $\varepsilon_{cell}(\lambda) = \alpha_{cell}(\lambda,\theta_{sun})$ is the emissivity of the silicon layer that is assumed independent of polar angle θ, even if the front surface of silicon is flat, because of its high refractive index that refracts the incident light very close to perpendicular inside the solar cell.

Funding

Disclosures

The authors declare no conflicts of interest.

References

1. W. Shockley and H. J. Queisser, "Detailed Balance Limit of Efficiency of p-n Junction Solar Cells," J. Appl. Phys. **32**(3), 510–519 (1961).
2. R. Couderc, M. Amara, and M. Lemiti, "In-Depth Analysis of Heat Generation in Silicon Solar Cells," IEEE J. Photovoltaics **6**(5), 1123–1131 (2016).
3. O. Dupré, R. Vaillon, and M. A. Green, "A full thermal model for photovoltaic devices," Sol. Energy **140**, 73–82 (2016).
4. S. Dubey, J. N. Sarvaiya, and B. Seshadri, "Temperature Dependent Photovoltaic (PV) Efficiency and Its Effect on PV Production in the World – A Review," Energy Procedia **33**, 311–321 (2013).
5. M. W. Davis, A. H. Fanney, and B. P. Dougherty, "Prediction of Building Integrated Photovoltaic Cell Temperatures," J. Sol. Energy Eng. **123**(3), 200–210 (2001).
6. E. Skoplaki and J. A. Palyvos, "On the temperature dependence of photovoltaic module electrical performance: A review of efficiency/power correlations," Sol. Energy **83**(5), 614–624 (2009).
7. D. Otth, R. R.-29th I. of E. S. Technical, and undefined 1983, "Assessing photovoltaic module degradation and lifetime from long term environmental tests," jpl.nasa.gov (n.d.).
8. H. G. Teo, P. S. Lee, and M. N. A. Hawlader, "An active cooling system for photovoltaic modules," Appl. Energy **90**(1), 309–315 (2012).
9. K. A. Moharram, M. S. Abd-Elhady, H. A. Kandil, and H. El-Sherif, "Enhancing the performance of photovoltaic panels by water cooling," Ain Shams Eng. J. **4**(4), 869–877 (2013).
10. A. Akbarzadeh and T. Wadowski, "Heat pipe-based cooling systems for photovoltaic cells under concentrated solar radiation," Appl. Therm. Eng. **16**(1), 81–87 (1996).
11. A. P. Raman, M. A. Anoma, L. Zhu, E. Rephaeli, and S. Fan, "Passive radiative cooling below ambient air temperature under direct sunlight," Nature **515**(7528), 540–544 (2014).
12. L. Zhu, A. P. Raman, and S. Fan, "Radiative cooling of solar absorbers using a visibly transparent photonic crystal thermal blackbody," Proc. Natl. Acad. Sci. U. S. A. **112**(40), 12282–12287 (2015).
13. L. Zhu, A. Raman, K. X. Wang, M. A. Anoma, and S. Fan, "Radiative cooling of solar cells," Optica **1**(1), 32 (2014).
14. Y. Lu, Z. Chen, L. Ai, X. Zhang, J. Zhang, J. Li, W. Wang, R. Tan, N. Dai, and W. Song, "A Universal Route to Realize Radiative Cooling and Light Management in Photovoltaic Modules," Sol. RRL **1**(10), 1700084 (2017).
15. W. Li, Y. Shi, K. Chen, L. Zhu, and S. Fan, "A Comprehensive Photonic Approach for Solar Cell Cooling," ACS Photonics **4**(4), 774–782 (2017).
16. B. Zhao, M. Hu, X. Ao, Q. Xuan, and G. Pei, "Comprehensive photonic approach for diurnal photovoltaic and nocturnal radiative cooling," Sol. Energy Mater. Sol. Cells **178**, 266–272 (2018).
17. A. Riverola, A. Mellor, D. Alonso Alvarez, L. Ferre Llin, I. Guarracino, C. N. Markides, D. J. Paul, D. Chemisana, and N. Ekins-Daukes, "Mid-infrared emissivity of crystalline silicon solar cells," Sol. Energy Mater. Sol. Cells **174**, 607–615 (2018).
18. T. J. Silverman, M. G. Deceglie, I. Subedi, N. J. Podraza, I. M. Slauch, V. E. Ferry, and I. Repins, "Reducing Operating Temperature in Photovoltaic Modules," IEEE J. Photovoltaics **8**(2), 532–540 (2018).
19. M. R. Vogt, H. Schulte-Huxel, M. Offer, S. Blankemeyer, R. Witteck, M. Köntges, K. Bothe, and R. Brendel, "Reduced Module Operating Temperature and Increased Yield of Modules with PERC Instead of Al-BSF Solar Cells," IEEE J. Photovoltaics **7**(1), 44–50 (2017).
20. R. Vaillon, O. Dupré, R. B. Cal, and M. Calaf, "Pathways for mitigating thermal losses in solar photovoltaics," Sci. Rep. **8**(1), 13163–9 (2018).
21. T. Saga, "Advances in crystalline silicon solar cell technology for industrial mass production," NPG Asia Mater. **2**(3), 96–102 (2010).
22. D. D. Smith, P. J. Cousins, A. Masad, S. Westerberg, M. Defensor, R. Ilaw, T. Dennis, R. Daquin, N. Bergstrom, A. Leygo, X. Zhu, B. Meyers, B. Bourne, M. Shields, and D. Rose, "SunPower's Maxeon Gen III solar cell: High efficiency and energy yield," in *2013 IEEE 39th Photovoltaic Specialists Conference (PVSC)* (IEEE, 2013), pp. 0908–0913.
23. K. R. McIntosh, J. N. Cotsell, J. S. Cumpston, A. W. Norris, N. E. Powell, and B. M. Ketola, "An optical comparison of silicone and EVA encapsulants for conventional silicon PV modules: A ray-tracing study," in *2009 34th IEEE Photovoltaic Specialists Conference (PVSC)* (IEEE, 2009), pp. 000544–000549.
24. E. D. Palik, *Handbook of Optical Constants of Solids. II* (Academic University, 1998).
25. U. Wurfel, A. Cuevas, and P. Wurfel, "Charge Carrier Separation in Solar Cells," IEEE J. Photovoltaics **5**(1), 461–469 (2015).
26. "Solar Spectral Irradiance: Air Mass 1.5," https://rredc.nrel.gov/solar/spectra/am1.5/.
27. F. J. Castano, D. Morecroft, M. Cascant, H. Yuste, M. W. P. E. Lamers, A. A. Mewe, I. G. Romijn, E. E. Bende, Y. Komatsu, A. W. Weeber, and I. Cesar, "Industrially feasible >19% efficiency IBC cells for pilot line processing," in *2011 37th IEEE Photovoltaic Specialists Conference* (IEEE, 2011), pp. 001038–001042.
28. T. Tiedje, E. Yablonovitch, G. D. Cody, and B. G. Brooks, "Limiting efficiency of silicon solar cells," IEEE Trans. Electron Devices **31**(5), 711–716 (1984).
29. M. A. Green, "Limits on the open-circuit voltage and efficiency of silicon solar cells imposed by intrinsic Auger processes," IEEE Trans. Electron Devices **31**(5), 671–678 (1984).

30. K. G. Svantesson and N. G. Nilsson, "The temperature dependence of the Auger recombination coefficient of undoped silicon," J. Phys. C: Solid State Phys. **12**(23), 5111–5120 (1979).

31. A. Richter, M. Hermle, and S. W. Glunz, "Reassessment of the limiting efficiency for crystalline silicon solar cells," IEEE J. Photovoltaics **3**(4), 1184–1191 (2013).

32. H. Steinkemper, M. Hermle, and S. W. Glunz, "Comprehensive simulation study of industrially relevant silicon solar cell architectures for an optimal material parameter choice," Prog. Photovoltaics Res. Appl. **24**(10), 1319–1331 (2016).

33. K. Misiakos and D. Tsamakis, "Accurate measurements of the silicon intrinsic carrier density from 78 to 340 K," J. Appl. Phys. **74**(5), 3293–3297 (1993).

34. P. P. Altermatt, "Models for numerical device simulations of crystalline silicon solar cells - A review," J. Comput. Electron. **10**(3), 314–330 (2011).

35. O. Breitenstein, "Understanding the current-voltage characteristics of industrial crystalline silicon solar cells by considering inhomogeneous current distributions," Opto-Electronics Rev. **21**(3), 259–282 (2013).

36. S. Roy Chowdhury and H. Saha, "Maximum power point tracking of partially shaded solar photovoltaic arrays," Sol. Energy Mater. Sol. Cells **94**(9), 1441–1447 (2010).

37. T. S. Safi and J. N. Munday, "Improving photovoltaic performance through radiative cooling in both terrestrial and extraterrestrial environments," Opt. Express **23**(19), A1120 (2015).

38. P. Singh, S. N. Singh, M. Lal, and M. Husain, "Temperature dependence of I–V characteristics and performance parameters of silicon solar cell," Sol. Energy Mater. Sol. Cells **92**(12), 1611–1616 (2008).

39. O. Dupré, R. Vaillon, and M. A. Green, "Physics of the temperature coefficients of solar cells," Sol. Energy Mater. Sol. Cells **140**, 92–100 (2015).

40. H. Steinkemper, I. Geisemeyer, M. C. Schubert, W. Warta, and S. W. Glunz, "Temperature-Dependent Modeling of Silicon Solar Cells-Eg, ni, Recombination, and VOC," IEEE J. Photovoltaics **7**(2), 450–457 (2017).

41. E. Rephaeli, A. Raman, and S. Fan, "Ultrabroadband Photonic Structures To Achieve High-Performance Daytime Radiative Cooling," Nano Lett. **13**(4), 1457–1461 (2013).

42. "IR Transmission Spectra | Gemini Observatory," http://www.gemini.edu/sciops/telescopes-and-sites/observing-condition-constraints/ir-transmission-spectra.

43. P. Wurfel, "The chemical potential of radiation," J. Phys. C: Solid State Phys. **15**(18), 3967–3985 (1982).

44. "The SunPower Maxeon ® Solar Cell Conventional Panel SunPower ® X-Series 12% More Power in Year 25 SunPower ® E-Series and X-Series Conventional Panel".

45. "Eagle 72M G2 – JinkoSolar US," https://jinkosolar.us/product/eagle-72m-g2/.

46. D. Wu, C. Liu, Z. Xu, Y. Liu, Z. Yu, L. Yu, L. Chen, R. Li, R. Ma, and H. Ye, "The design of ultra-broadband selective near-perfect absorber based on photonic structures to achieve near-ideal daytime radiative cooling," Mater. Des. **139**, 104–111 (2018).

47. M. C. C. de Oliveira, A. S. A. Diniz Cardoso, M. M. Viana, V. de F, and C. Lins, "The causes and effects of degradation of encapsulant ethylene vinyl acetate copolymer (EVA) in crystalline silicon photovoltaic modules: A review," Renewable Sustainable Energy Rev. **81**, 2299–2317 (2018).

48. W. J. Yang, Z. Q. Ma, X. Tang, C. B. Feng, W. G. Zhao, and P. P. Shi, "Internal quantum efficiency for solar cells," Sol. Energy **82**(2), 106–110 (2008).

49. D. C. Jordan and S. R. Kurtz, "Photovoltaic Degradation Rates-an Analytical Review," Prog. Photovoltaics Res. Appl. **21**(1), 12–29 (2013).

50. Z. Zhou, Z. Wang, and P. Bermel, "Radiative cooling for low-bandgap photovoltaics under concentrated sunlight," Opt. Express **27**(8), A404 (2019).